Effect of Structure on Response of a Three-Dimensional-Printed Photopolymer-Particulate Composite Under Intermediate Strain Rate Loading

Amirreza Keyhani
The George W. Woodruff
School of Mechanical Engineering,
Georgia Institute of Technology,
Atlanta, GA 30332-0405
e-mail: akeyhani3@gatech.edu

Min Zhou[1]
The George W. Woodruff
School of Mechanical Engineering,
School of Materials Science and Engineering,
Georgia Institute of Technology,
Atlanta, GA 30332-0405
e-mail: min.zhou@gatech.edu

The thermo-mechanical response of an additively manufactured photopolymer-particulate composite under conditions of macroscopic uniaxial compression without lateral confinement at overall strain rates of 400–2000 s^{-1} is studied. The material has a direct-ink-written unidirectional structure. Computations are performed to quantify the effects of microstructure attributes including anisotropy, defects, and filament size on localized deformation, energy dissipations, and temperature rises. To this effect, an experimentally informed Lagrangian finite element framework is used, accounting for finite-strain elastic–plastic deformation, strain-rate effect, failure initiation and propagation, post-failure internal contact and friction, heat generation due to friction and inelastic bulk deformation, and heat conduction. The analysis focuses on the material behavior under overall compression. Despite relatively low contribution to overall heating, friction is localized at fracture sites and plays an essential role in the development of local temperature spikes unknown as hotspots. The microstructural attributes are found to significantly affect the development of the hotspots, with local heating most pronounced when loading is transverse to the filaments or when the material has higher porosities, stronger inter-filament junctions, or smaller filament sizes. Samples with smaller filament sizes undergo more damage, exhibit higher frictional dissipation, and develop larger hotspots that occur primarily at failure sites. [DOI: 10.1115/1.4048050]

Keywords: photopolymer-particulate composite, multi-physics finite element simulations, dynamic loading, thermo-mechanical analysis, energy dissipation

1 Introduction

Additive manufacturing (AM) or 3D-printing provides an opportunity for functionally tailoring energetic materials (EM) for specific applications [1–4]. As a result, energetic constituents have been incorporated into conventional 3D-printing techniques including electrospray deposition (ESD) [5–9] and direct ink writing (DIW) [10,11] to create energetic materials for different purposes. DIW is capable of printing high solids-loaded (85 vol%) composites [12] and tailoring material properties through structure design [13]. DIW has been widely used with photopolymers. These light-sensitive polymers, oligomers, or monomers crosslink and solidify upon exposure to light of specific wavelengths such as those in the ultraviolet (UV) regime. UV-curable photopolymers provide low viscosities, allowing for 3D-printing of high solids-loaded particulate energetic composites. Unfortunately, 3D-printing processes also result in inherent heterogeneities, anisotropic behaviors, and poor mechanical properties [14,15]. Microstructure heterogeneities, defects, and anisotropy control the performance of materials under loading [16–21]. Therefore, it is necessary to systematically quantify the role of microstructure attributes of additively manufactured energetic materials (AMEMs) subjected to various loading conditions including in the dynamic regime in order to tailor the materials for applications.

UV-cured 3D-printed photopolymers show orientation-dependent anisotropic elastic properties and failure [22]. To account for anisotropic behavior of 3D-printed photopolymers, a transversely anisotropic continuum model was developed [23] based on isotropic hyperelastic and viscoplastic models for polymers [24,25]. This model does not account for microstructure morphology and heterogeneities. To understand the behavior of AMEMs under dynamic/shock loading, it is necessary to explicitly account for print structures and heterogeneities. The orientation-dependent dynamic/shock responses of a 3D-printed photopolymer-particulate composite have been the subject of recent studies [26,27]. This material mimics some attributes of AMEMs. This AMEM simulant is unidirectionally printed using DIW of a high solids-loaded photopolymer and cured under UV-light exposure. Wanger et al. [26] analyzed the shock compression response of the material in different directions. X-ray phase contrast imaging (PCI) was used to track features across the observed shock front and determine the shock velocity versus particle velocity equation of state (EOS). Keyhani and Zhou [27] experimentally analyzed the thermal and mechanical responses of the material to dynamic loading at an average strain rate of ~310 s^{-1}, using a recently developed novel capability for simultaneous measurement of temperature and deformation fields [28]. This technique enables simultaneous recording of the temperature field and the deformation field with micrometer spatial and microsecond temporal resolutions. Mesoscale computations were also performed to quantify the physics captured in the experiments.

Built upon these recent experimental and computational studies [26,27], this paper further analyzes the mesoscale thermo-mechanical response of the material. The analysis here focuses on the effects of microstructure, porosity, inter-filament strength, and filament size on the overall behavior at strain rates of 400–2000 s^{-1}. The computations account for the AM print structure,

[1]Corresponding author.

Contributed by the Applied Mechanics Division of ASME for publication in the Journal of Applied Mechanics. Manuscript received July 4, 2020; final manuscript received August 6, 2020; published online September 2, 2020. Assoc. Editor: Yonggang Huang.

finite-strain inelastic deformation, arbitrary crack initiation and propagation, contact and friction at crack surfaces, inelastic and frictional heat generation, and heat conduction. The framework is implemented in the ABAQUS/EXPLICIT 2018 package. Most material constitutive parameters are obtained from independent experiments or determined using experimental data in the literature.

2 Material and Microstructure

The samples are computationally generated based on scanned images of the real material, which is manufactured using DIW of a high solids-loaded photopolymer and cured under UV-light exposure. The material mimics some attributes of additive manufactured energetic materials. Figure 1(*a*) shows the external structure of such a material block. Details of the material microstructure and constituents are presented in Refs. [26,27], and therefore not repeated here. Figure 1(*b*) shows a computationally generated sample, illustrating the print structure and the internal defects including inter-filament surfaces and voids. The printer nozzle producing the filaments has a diameter of 1.2 mm; however, the printed filaments have approximately oval cross-sectional shapes due to setting. Inter-filament voids account for ∼3% of the sample volume. The size of the computational model is $5\times5\times5$ mm, large enough to capture at least three layers of the print structure.

To account for the process-inherent heterogeneities in the material, an approach involving the use of different bulk constituents is taken. Specifically, the microstructure consists of three different constituents, one for the filaments, another for the inter-filament surfaces, and a third for the inter-filament voids, as shown in Fig. 1(*b*). Among the filaments, three groups with differing properties (as indicated by the three different colors) are used to account for random fluctuations in the overall properties of the filament material. The elastic properties of each group are selected such that the overall elastic properties at the sample level match experimental measurements in both the longitudinal and transverse directions. The determination of the three sets of properties follows the Voigt upper bound and the Reuss lower bound [29], i.e.,

$$\left.\begin{aligned}\phi_L &= \sum_{i=1}^{n} v_i\phi_i \\ \phi_T &= \left[\sum_{i=1}^{n} v_i/\phi_i\right]^{-1}\end{aligned}\right\} \tag{1}$$

where ϕ_i and v_i are the property value and the volume fraction of constituent i, respectively, and $n=5$ accounting for the three groups of filaments, the interfaces, and the voids. ϕ_L and ϕ_T are the overall property values at the macroscale in the longitudinal and transverse orientations, respectively. To phenomenologically account for the effects of voids at inter-filament junctions, the material properties are locally decreased to fractions of those in the filaments. The macro longitudinal and transverse properties are obtained from quasi-static tests and listed in Table 1.

Table 1 Mechanical properties of the additively manufactured photopolymer-particulate composite in longitudinal and transverse orientations

Orientation	E (GPa)	σ_c(MPa)	ε_c (%)
Longitudinal (y)	2.54 ± 0.05	23.95 ± 4.50	1.15 ± 0.18
Transverse (x and z)	0.97 ± 0.19	21.64 ± 3.02	2.57 ± 0.76

Note: E is the Young's modulus, σ_c is the yield stress in compression, and ε_c is the yield strain in compression.

3 Governing Equations and Constitutive Relations

3.1 Governing Equations and Finite-Strain Elastic–Plastic Constitutive Model. The governing equations are balance of momentum and conservation of energy in the forms of

$$\nabla\cdot\boldsymbol{\sigma} = \rho\ddot{\mathbf{u}} \tag{2}$$

and

$$\rho c_v\frac{\partial T}{\partial t} = k\nabla^2 T + \dot{W}^P + \dot{W}^F \tag{3}$$

where $\nabla = \partial/\partial x\mathbf{i} + \partial/\partial y\mathbf{j} + \partial/\partial z\mathbf{k}$ is the gradient operator in which ∂ denotes partial derivative, $\boldsymbol{\sigma}$ is the Cauchy stress tensor, ρ is the mass density, $\ddot{\mathbf{u}}$ is the acceleration, T is the temperature, c_v is the specific heat and estimated to be 1500 $\mathrm{Jkg^{-1}K^{-1}}$, and k is the thermal conductivity. Implied in Eq. (3) is Fourier's law of conduction. $\dot{W}^P = \boldsymbol{\sigma}:\mathbf{D}^P$ and $\dot{W}^F$ are the rates of plastic work and frictional dissipation per unit volume, respectively. Here, $\mathbf{D}^P$ is the plastic part of the rate of deformation tensor. The kinematic relations for the elastic–plastic deformation are presented in Refs. [20,27,30].

The linear Drucker–Prager pressure-dependent (DP) model is used to describe the yield and the plastic flow behavior [31]

$$\left.\begin{aligned}\sigma_e - \sigma_H\tan\beta - \left(1-\frac{1}{3}\tan\beta\right)\bar{\sigma}_c = 0 \\ \tan\beta = 3\frac{m-1}{m+1}\end{aligned}\right\} \tag{4}$$

where σ_e is the von Mises equivalent stress, $\sigma_H = (\sigma_{11}+\sigma_{22}+\sigma_{33})/3$ is the hydrostatic stress, β is the friction angle of the material in the meridional stress plane, and $m=\sigma_c/\sigma_t$ in which σ_c and σ_t are the yield points in compression and tension, respectively. The DP model is used for polymers with $m\simeq1.3$ [32]. The Jonson–Cook constitutive model is used to account for the effects of strain, strain rate, and temperature on the flow stress in compression ($\bar{\sigma}_c$)

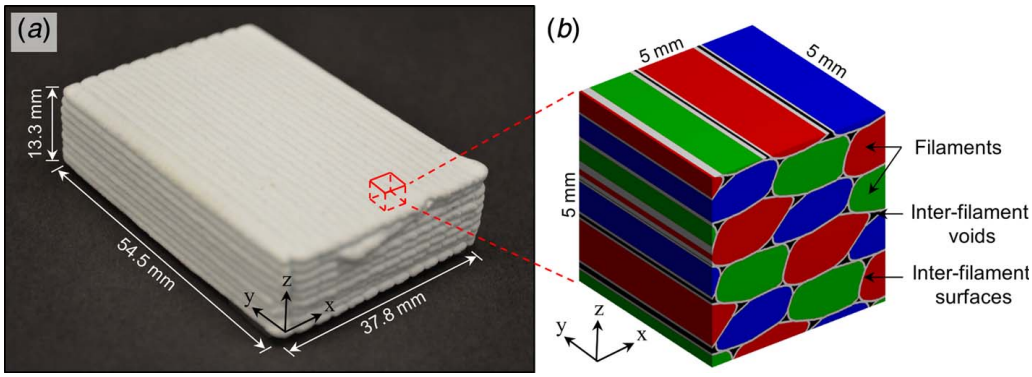

Fig. 1 (*a*) The as-printed material block showing orientation notations aligned along the print direction and (*b*) illustration of AM printing pattern and computational model

Table 2 Material property sets for the reference microstructure

Material set	ρ (gr/cm^3)	E (GPa)	σ_c (MPa)	ε_c (%)	$\bar{\varepsilon}_D^{pl}$(%)	$\delta_f = L_E \cdot \bar{\varepsilon}_f^{pl}$(mm)
Filaments-set 1 (blue filaments)	1.6	0.5	15.0	3.0	12	0.0188
Filaments-set 2 (green filaments)	1.6	2.5	22.5	0.9	12	0.0188
Filaments-set 3 (red filaments)	1.6	4.5	30.0	0.7	12	0.0188
Inter-filament surfaces	1.1	2.5	22.5	0.9	8	0.0125
Inter-filament voids	0.5	0.5	15.0	3.0	4	0.0063

in the form of

$$\bar{\sigma}_c = [A + B(\bar{\varepsilon}^{pl})^n]\left[1 + C\ln\left(\frac{\dot{\bar{\varepsilon}}^{pl}}{\dot{\varepsilon}_0}\right)\right]\left[1 - \left(\frac{T - T_0}{T_m - T_0}\right)^m\right] \quad (5)$$

where the first bracket represents the effect of strain hardening, the second bracket accounts for the effect of strain rate, and the last bracket denotes the effect of temperature. Here, $\bar{\varepsilon}^{pl}$ is the equivalent plastic strain, $\dot{\bar{\varepsilon}}^{pl}$ is the equivalent plastic strain rate, $\dot{\varepsilon}_0$ is the reference strain rate, T is the temperature, T_0 is the reference temperature, and T_m is the melting temperature. A, B, c, n, and m are material parameters. In this paper, the effects of strain hardening and temperature are not considered since the temperature increases are relatively low and the material show negligible strain hardening under conditions analyzed ($B = 0$, $T \approx T_0$). Under this condition, $A = \sigma_c$ which is the yield strength in compression corresponding to the reference strain rate $\dot{\varepsilon}_0$, and $C = 0.005$ based on a qualitative comparison of the results from the computations and the experiments.

The Mie–Grüneisen equation of state (EOS) is used to describe the volumetric behavior

$$p = -\sigma_H = \frac{\rho_0 c_0^2 \eta}{(1 - s\eta)^2}\left(1 - \frac{\Gamma_0 \eta}{2}\right) + \Gamma_0 \rho_0 E_m \quad (6)$$

where ρ_0 is the density in the reference configuration, $\eta = 1 - \rho_0/\rho$ is the nominal volumetric compressive strain in which ρ is the instantaneous density, Γ_0 is Grüneisen's gamma at the reference state and for polymers $\Gamma_0 \simeq 1$, E_m is the internal energy per unit mass, and c_0 and s are the constants in the linear relationship between the shock velocity U_s and the particle velocity U_p, $U_s = c_0 + sU_p$. For the material analyzed, $U_s = 2315.4 + 1.905U_p$, and the orientation-dependency of $U_s - U_p$ relationship is negligible [26].

3.2 Damage Initiation, Failure, and Post-Failure Contact and Friction. To account for arbitrary patterns of fracture, a phenomenological damage criterion proposed by Hooputra et al. [33] is used. The damage model assumes that the equivalent plastic strain at the onset of damage is $\bar{\varepsilon}_D^{pl}$. The evolution of damage is based on fracture energy per unit area dissipated during the damage process, and the equivalent plastic strain at failure is $\bar{\varepsilon}_f^{pl}$. $\bar{\varepsilon}_D^{pl}$ and $\bar{\varepsilon}_f^{pl}$ are the input parameters and selected based on experimental results. When the failure criterion is met in an element, the element fails, and the surfaces of the adjacent elements connected to the failed element turn into free surfaces. A penalty force algorithm is used to achieve proper contact at free surfaces or fracture sites. The Coulomb friction law is used to determine the stick-slip states of the sliding surfaces in contact and to estimate frictional heating. The frictional heating rate over volume ΔV with surface ΔS is

$$\dot{W}^F = \frac{1}{\Delta V}\int_{\Delta S} \mu \sigma_n v_{rel} dS \quad (7)$$

where μ is the coefficient of friction and selected to be 0.5 for all surfaces in contact, σ_n is the normal stress between the surface pair in contact, and v_{rel} is the relative sliding velocity of contact pairs.

To reduce mesh dependence associated with material failure, a characteristic element length L_E is incorporated in ABAQUS. An equivalent displacement at failure is introduced such that $\delta_f = L_E \cdot \bar{\varepsilon}_f^{pl}$. For three-dimensional elements, L_E is the cube-root of the element volume. An alternative solution to mitigate the effects of mesh sensitivity is a non-local approach (not used here), which defines a characteristic length L_M as a material property [34,35]. The values of properties of each constituent are listed in Table 2.

3.3 Loading Configuration. As shown in Fig. 2, the material is uniaxially compressed between two rigid surfaces (front and back) without lateral (upper and lower, left and right) confinement. Loading is in the horizontal direction, with the left (front) surface moving at velocities of 2–10 m/s toward the right (back) surface which is stationary at all time, resulting in overall strain rates of 400–2000 s^{-1}. This loading configuration mimics the loading conditions in the split-Hopkinson pressure bar (SHPB) or Kolsky bar experiments reported in Refs. [27,28].

4 Results

Three sets of simulations are performed to quantify the effects of print structure, defects (voids and interfaces), and filament size on the thermo-mechanical response of the material to dynamic loading. In the first set, the behavior of the reference microstructure (1.2 mm size filaments and 3 vol% inter-filament voids) is analyzed in 4 (x, y (filament), z (build), and xy-diagonal) orientations. In the second set, variants of the reference microstructure are analyzed with 0, 3, and 6 vol% voids while the 1.2 mm size for the filaments is maintained. In addition, two other cases with stronger and weaker inter-filament surfaces with respect to that in the reference microstructure are analyzed. In the third set, three samples are analyzed with filament sizes of 0.8, 1.2, and 1.6 mm. The three cases have

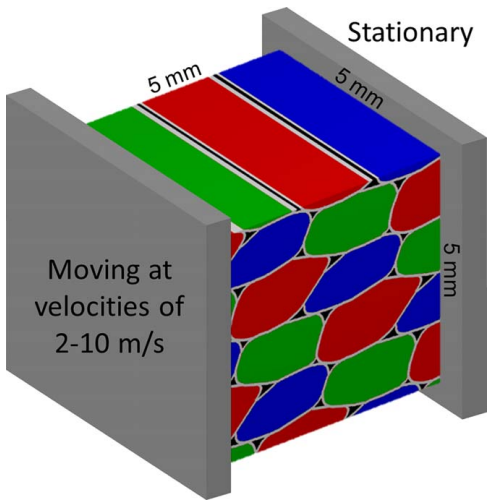

Fig. 2 Loading configuration mimicking the conditions of the experiments reported in Refs. [27,28]

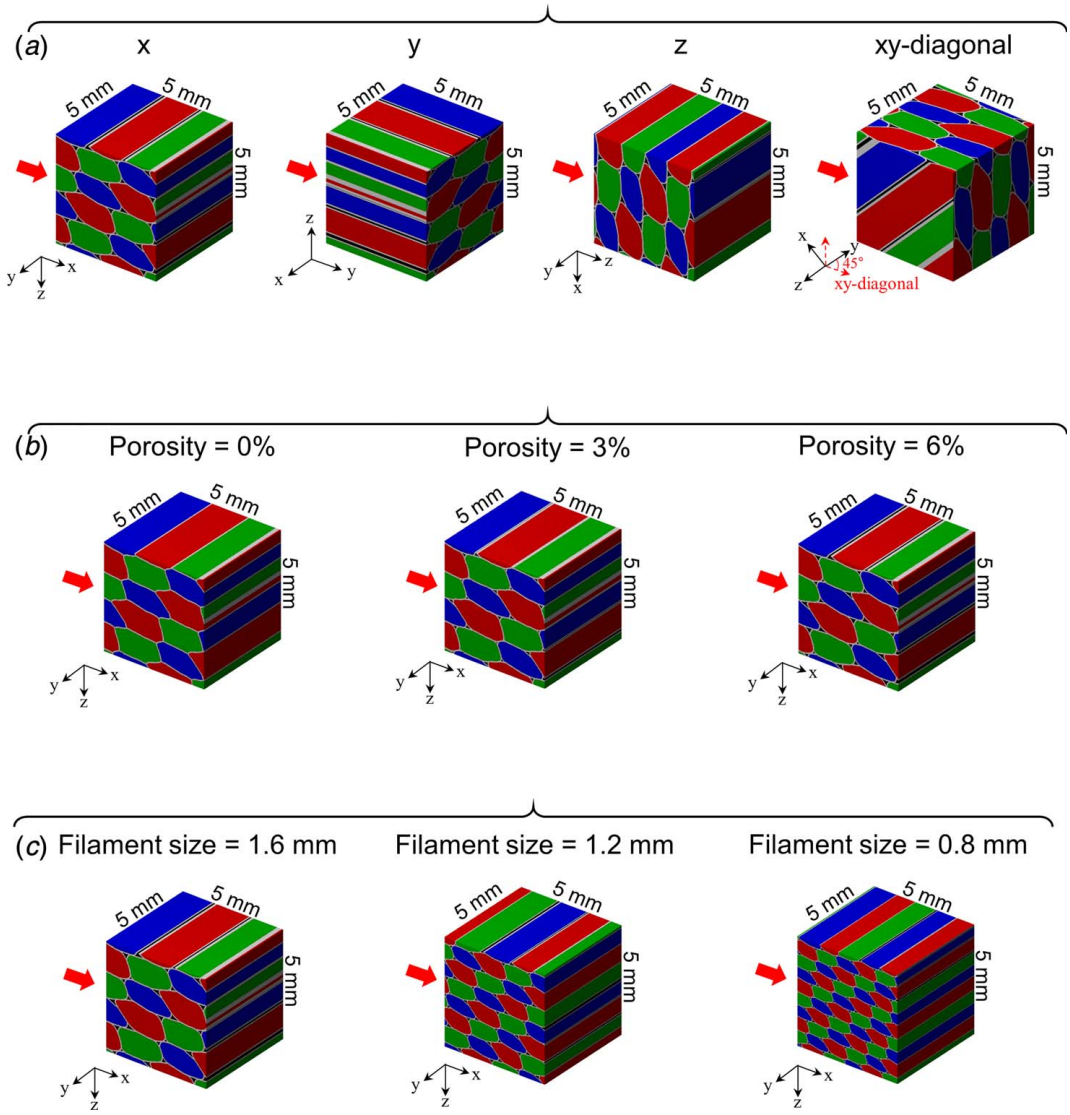

Fig. 3 Simulation sets and illustrations of impact directions with respect to AM printing pattern and microstructure morphologies: (*a*) loading along various orientations with respect to the material print structure, (*b*) porosities of 0–6 vol%, and (*c*) filament sizes of 0.8–1.6 mm

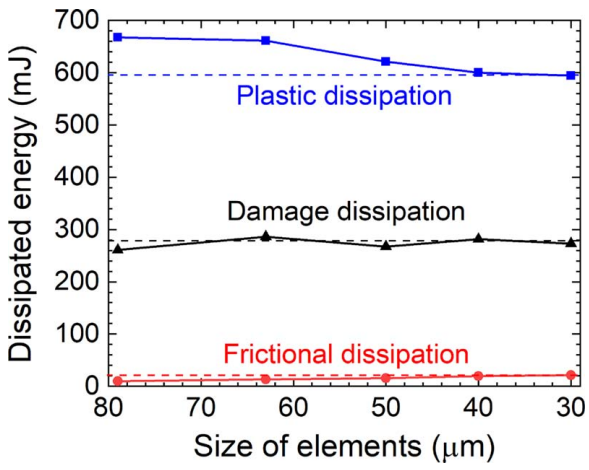

Fig. 4 Dissipated energy levels as a function of elements sizes

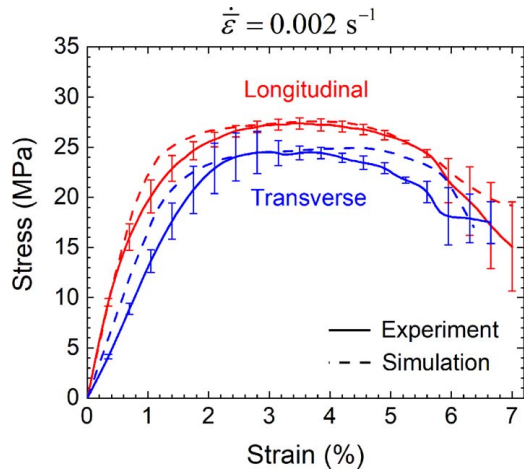

Fig. 5 Comparison of measured and calculated strain–stress curves for longitudinal and transverse orientations. The error bars show the variation of the overall stress levels measured for multiple samples.

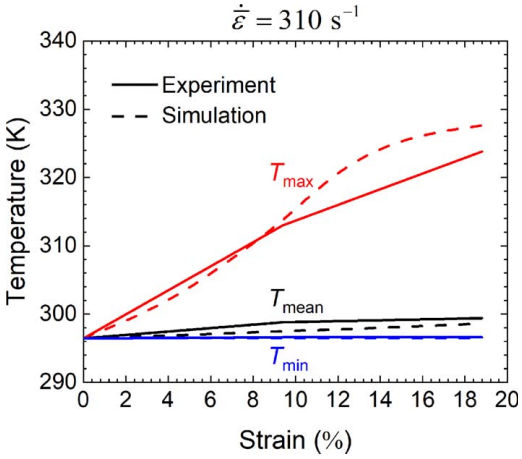

Fig. 6 Comparison of measured and calculated lowest, mean, and highest temperature levels (T_{min}, T_{mean}, and T_{max}) as a function of overall strain [$\Delta L/L_0$(%)]

the same level of porosity of 3% voids by volume. In the latter two simulation sets, the samples are subjected to dynamic loading in the x direction in which the effects of AM microstructure are most pronounced. Figures 3(*a*)–3(*c*) summarize the microstructures of the samples used in all simulation sets.

4.1 Mesh-Size Convergence Analysis. To evaluate the mesh sensitivity, the size of elements is varied over a range of 31–79 μm. Figure 4 shows the energy dissipated through plastic deformation, friction, and damage as functions of the element size. The solution reaches convergence for an element size of 31 μm. At this size, the samples are meshed with $\sim 4 \times 10^6$ cubic elements. To prevent shear locking and counteract volumetric locking, reduced integration elements are used (specified with C3D8RT in ABAQUS). The selection of a certain mesh size in conjunction with the implementation of a characteristic length equal to the cube-root of the element volume provides an approximately non-local basis for damage initiation and evolution.

4.2 Experimental Validation. To ensure the computational model captures the essential physics of the material, the results obtained from computations are compared with experimental measurements. Figure 5 compares the stress–strain curves obtained from the computations and experiments under quasi-static loading conditions. Under both longitudinal and transverse loading, the calculated overall stress levels are in very good agreement with the experimentally measured stress levels. Specifically, the computations closely predict the onset of plastic deformation and failure. Figure 6 compares the lowest, average, and highest temperature levels obtained from the simulations and corresponding dynamic experiments [27]. The computations and experiments are at an overall strain-rate level of $\sim 310\ s^{-1}$. The in situ experimental measurements were performed in the SHPB environment with an integrated system of high-speed visible and infrared imaging [27,28]. The calculated temperatures are in very good agreement with the experimentally measured temperatures, with the error being only ~ 3.9 K ($\sim 14.0\%$) in the highest temperatures. These agreements provide a form of validation of the computational model.

4.3 Orientation Dependence of Behavior. An experimental study of the mechanical and thermal responses of the material to dynamic loading in various orientations was reported in Ref. [27]. The overall strain rate is $\sim 310\ s^{-1}$. Here, the orientation-dependency of the material response is further investigated over strain rates of 400–2000 s^{-1}. Loading along four orientations (x, y, z, and xy-diagonal, with filaments oriented in the y direction) is analyzed. Figure 7(*a*) shows how damage evolves in the samples at a strain rate of 1200 s^{-1}. Damage initiates at the filament junctions and propagates through the filaments. The sample experiences only minor damage at $\bar{\varepsilon} = 0.35$ when loaded in the y direction, while the sample shows extensive damage when loaded at other

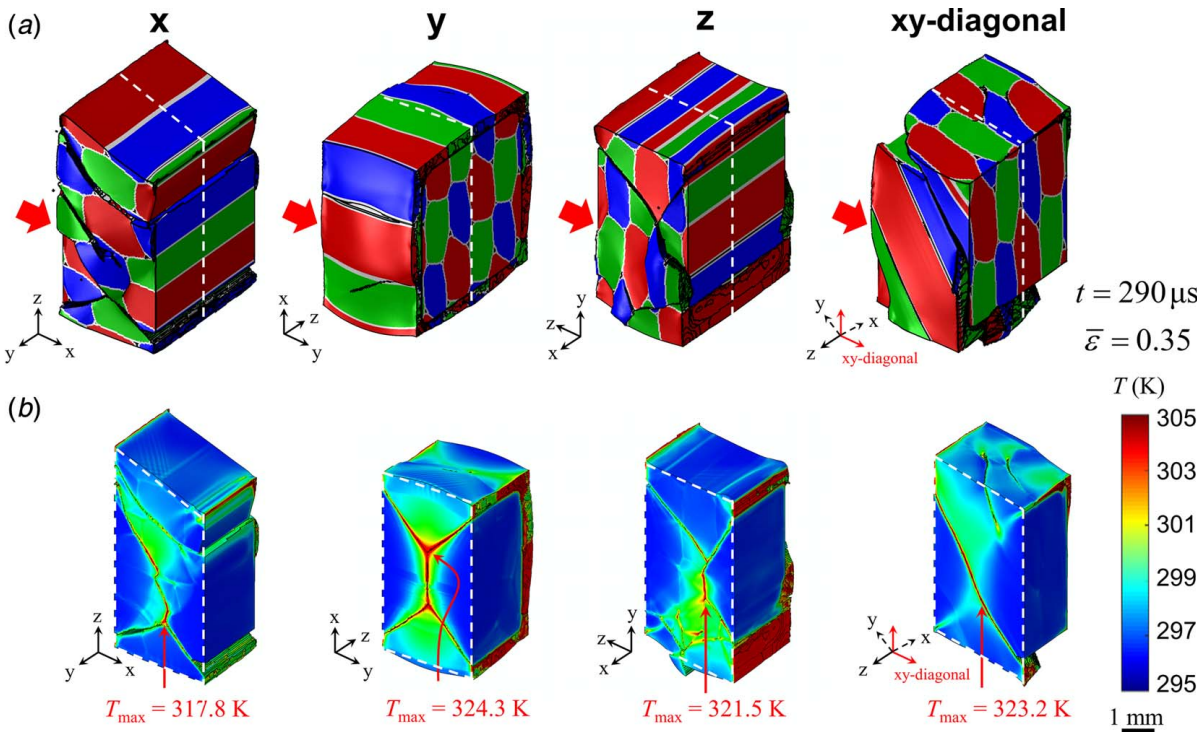

Fig. 7 (*a*) Fracture evolution in the samples loaded in various orientations and (*b*) temperature distributions for loading along *x* direction, *y* (filament) direction, *z* (build) direction, and *xy*-diagonal direction

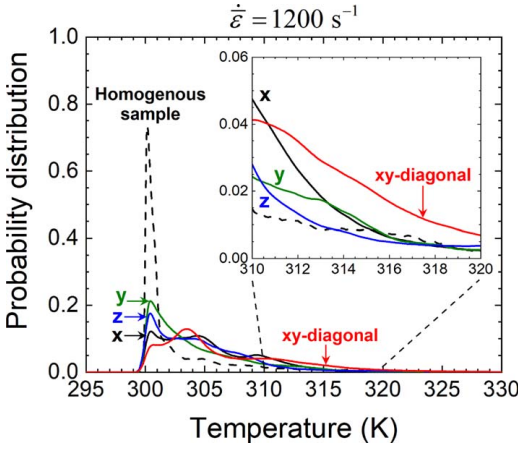

Fig. 8 Temperature distributions of the samples loaded in various directions and subjected to a strain rate of 1200 s^{-1}

orientations. Figure 7(*b*) shows the temperature fields in the samples at $\bar{\varepsilon} = 0.35$ ($t = 290\ \mu s$). Temperature spikes are located at or near fracture sites. Figure 8 quantifies the spatial distribution of temperature corresponding to Fig. 7(*b*). Loading in the *xy*-diagonal direction results in the highest temperatures. In contrast, loading in other orientations yields less concentrated heating and higher fractions of the material participate at the lower end of the temperature range. The homogeneous sample shows the lowest temperature levels.

Figures 9(*a*) and 9(*b*) quantify contributions to dissipation by plastic deformation (W_P) and fiction (W_F) as functions of overall strain rate and loading orientation at $\bar{\varepsilon} = 0.35$. Both W_P and W_F increase as the loading rate increases, as expected. Frictional dissipation is more sensitive to the loading rate and increases 18.9 – 27.1% as the loading rate increases from 400 to 2000 s^{-1}, but plastic dissipation is less sensitive and only increases 1.7 – 6.4% over the same loading rate range. Loading in the *y* direction results in the least damage (see Fig. 7(*a*)) and the highest level of stress carried by the material, leading to the highest plastic dissipation among all loading directions. In contrast, loading in the *xy*-diagonal direction leads to the highest damage and fracture, resulting in the highest frictional dissipation. Despite only 1 – 4% contribution to total heating, friction dissipation is localized at fracture sites and plays an important role in the development of hotspots or sites of localized temperature increases. Figure 8 shows temperature distributions for all loading orientations. Although loading in the *xy*-diagonal direction yields the lowest overall plastic dissipation, but it results in the highest level of frictional dissipation and the highest fraction of material volume in the peak temperature range of 310–320 K. Loading in the y direction leads to the lowest frictional dissipation and the lowest fraction of material volume in the peak temperature range despite the highest overall dissipation in the direction. The interplay between plasticity and friction is discussed in Ref. [27].

4.4 Effect of Void Volume Fraction and Inter-Filament Strength. Voids and inter-filament surfaces are the two types of defects in the material. These defects control the overall response to dynamic loading. To quantify the effects of void fraction and interfacial strength, variants of the reference sample are analyzed. In one set of simulations, the porosity of the samples varied between 0 and 6 vol%. The porosity of the reference sample is 3 vol%. Two other samples are generated based on the reference sample with the amounts of voids of 0 vol% in one and 6 vol% in the other. The material constituent properties and the overall microstructure morphology are the same in all three samples.

Figure 10 shows the overall stress–strain curves of the three samples at a strain rate of 1200 s^{-1}. The samples with lower porosities show higher levels of stress carried up to the strain of 26% and all cases show approximately equal levels of stress after that. The variations in overall stress levels result from damage initiation and evolution. In general, damage initiates from inter-filament junctions and propagates along shear bands. Higher porosity levels lead to earlier damage initiation. Figure 11(*a*) shows damage initiates at $\bar{\varepsilon} \simeq 0.05$ for 6% porosity but at $\bar{\varepsilon} \simeq 0.08$ for 0% porosity. The overall damage dissipation levels begin to converge at $\bar{\varepsilon} \simeq 0.22$ and become approximately equal at $\bar{\varepsilon} \simeq 0.36$. In the homogeneous sample, damage initiates at $\bar{\varepsilon} \simeq 0.14$, which is later than in the heterogeneous samples. Higher porosities lead to higher levels of damage at earlier stages of loading and higher overall frictional dissipation, as shown in Fig. 11(*b*). Figure 12 shows the temperature distributions. The samples with higher porosities exhibit higher proportions of volume with temperatures higher than 305 K. The samples with higher levels of frictional dissipation show higher material proportions with high temperatures. The difference in temperature distributions between the sample with no porosity and the samples with porosities is pronounced. In contrast, the difference in the temperature distributions among the samples with different levels of porosity is relatively minor. This fact shows that the rate

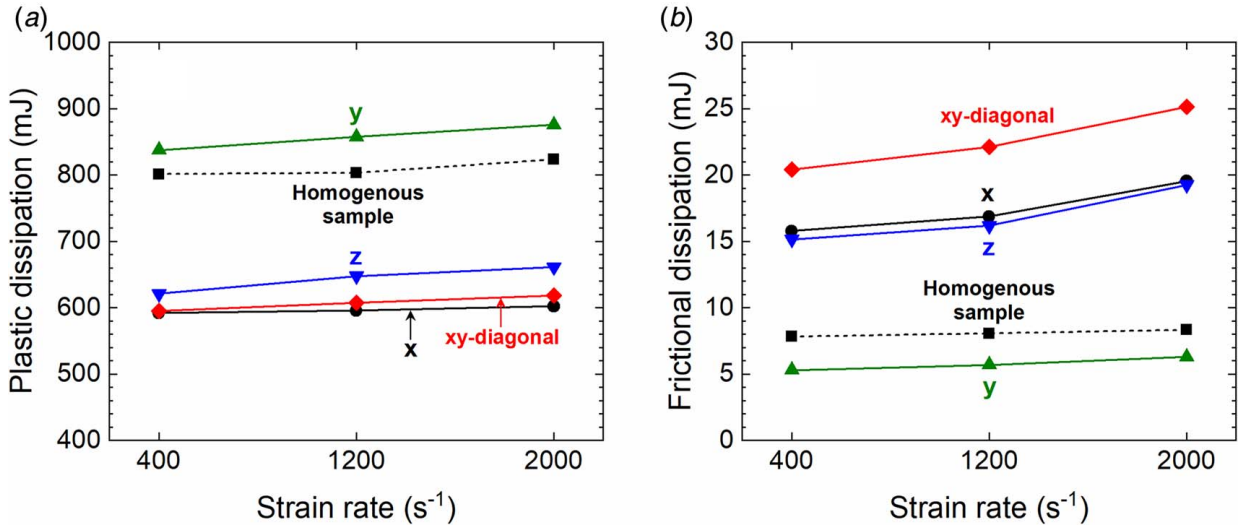

Fig. 9 Dissipations from (*a*) plastic deformation and (*b*) friction as a function of strain rate at $\bar{\varepsilon} = 0.35$

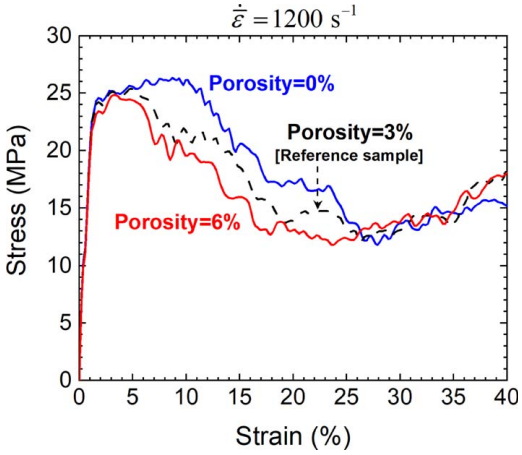

Fig. 10 Strain–stress curves of the samples with porosities of 0–6 vol%

of hotspot development with respect to the porosity is higher at lower porosity levels.

In another set of simulations, three samples with various levels of interfacial strength are analyzed. Specifically, three levels of $\bar{\varepsilon}_f^{pl}$ (plastic strain at failure) for inter-filament surfaces are used. In the reference sample, the ratio between $\bar{\varepsilon}_f^{pl}$ at inter-filament surfaces and at in the filaments is 0.67 ($R = 0.67$). This level is referred to as "intermediate strength." The samples with $R = 0.34$ and $R = 1$ are referred to as having "low-strength" and "high-strength" inter-filament surfaces throughout this paper. When $R = 1$, the plastic strain levels at the onset of damage ($\bar{\varepsilon}_D^{pl}$) and failure ($\bar{\varepsilon}_f^{pl}$) are equal to those in the filaments. Table 3 list the values of parameters used for the three inter-filament strength levels. Here, particles and particle-matrix interfaces are not explicitly modeled. The phenomenological approach for capturing the effects of interfaces and the related parameters are calibrated using experimental data reported in Ref. [22]. It is useful to note that, for traditionally manufactured energetic materials, Prakash et al. [36] and Olokun et al. [37] measured directly the properties of particle-matrix interfaces. Such direct measurements would be much desired and very useful, if they can be made for AM materials like the materials studied here.

Figure 13 shows the overall stress–strain curves of the samples with various inter-filament strength levels. The inter-filament strength level determines the overall integrity of the sample under loading. The samples with higher levels of inter-filament strength experience lower levels of damage and carry higher levels of stress. Figure 14 shows fracture patterns and temperature fields on cross sections parallel to the loading direction. Higher levels of R result in lower levels of fracture. The hotspots are at or near crack surfaces. The sample with $R = 1$ shows relatively larger hotspots at fracture sites. This fact can be quantitatively seen in Fig. 15, where the temperature distributions in the samples are shown. Compared with the samples with $R = 0.34$ or 0.67, a higher proportion of the sample with $R = 1$ is approximately at or close to the initial temperature (300–302 K). This is due to the fact that this sample undergoes a lower level of fracture; therefore, there are fewer sites for frictional sliding and consequent frictional heating. However, the $R = 1$ case shows a higher proportion with temperatures higher than 312 K. The peak temperature values are primarily controlled by localized frictional heating. The frictional heating rate increases as normal stress increases (see Eq. (7)). The samples with higher levels of inter-filament strength show lower levels of fracture and sustain a higher level of stress. Therefore, the fracture sites in these samples undergo more intense frictional heating as a result of the higher levels of stress.

4.5 Effect of Filament Size. Filament size is an important printing parameter which can be used to tailor the thermo-mechanical response of printed materials. Here, we analyze three samples with filament sizes of 0.8 mm, 1.2 mm, and 1.6 mm. These samples are loaded in the x direction (perpendicular to the filaments) for which the role of the AM microstructure is more pronounced. The strain rates are in the range of 400–2000 s^{-1}. Figures 16(*a*) and 16(*b*) show fracture patterns and temperature fields at a strain rate of 1200 s^{-1}, respectively. The samples with smaller filament sizes show more damage and higher temperature spikes at the fracture sites, owing to the fact that there are more interfacial heterogeneities. Figure 17 shows the temperature distributions in the samples corresponding to Fig. 16. The samples with smaller filament sizes show higher proportions at temperature levels higher than 314 K.

Figure 18 shows the ratios of damage dissipation in the heterogeneous AM samples to that in the homogenized sample (W_D/W_D') as a function of overall strain rate. The inherent heterogeneities as a result of the layer-by-layer build process lead to localized deformation and earlier damage initiation. Therefore, their dissipation levels are higher than that in the homogenous sample (i.e., $W_D/W_D' > 1$). The results show that the effect of

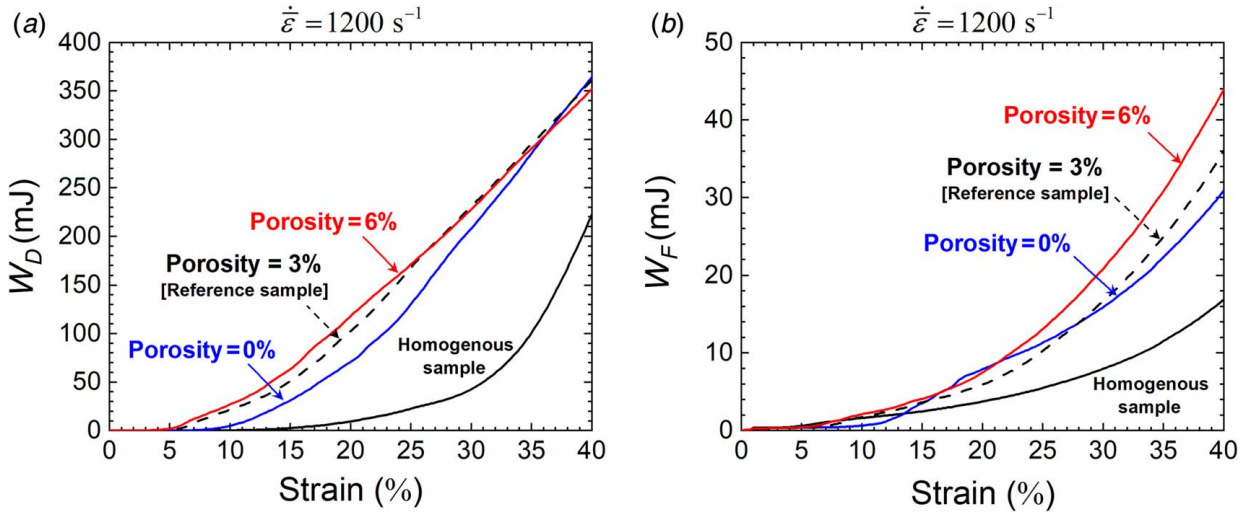

Fig. 11 Dissipations from (*a*) damage dissipation (W_D) and (*b*) friction (W_F) as a function of overall strain for the samples with porosities of 0–6 vol%

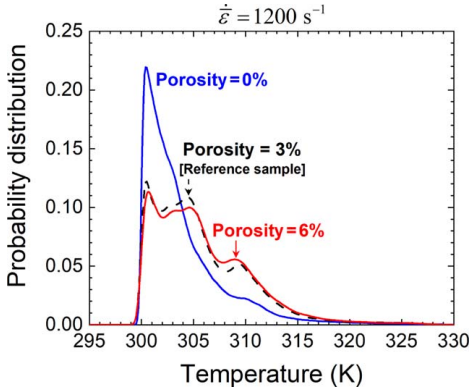

Fig. 12 Temperature distributions in the samples with porosities of 0–6% at $\bar{\varepsilon} = 0.35$

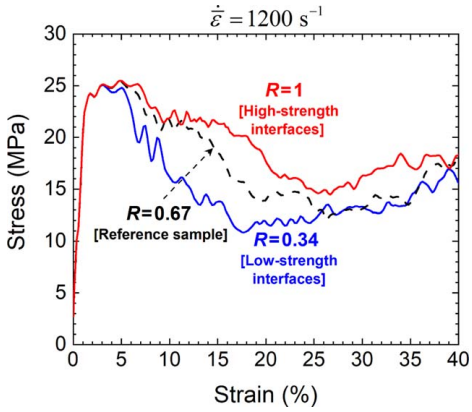

Fig. 13 Strain–stress curves of the samples with various inter-filament strength levels

microstructure is more pronounced at higher loading rates. For the reference sample, W_D/W'_D increases from ~3.9 to ~6.5 as the loading rate increases from 400 s^{-1} to 2000 s^{-1}. The samples with smaller filament sizes show higher levels of damage. This due to the fact that the samples with smaller filament sizes contain higher densities of inter-filament surfaces, which are weaker than filaments and dominate the onset of damage. The results also show W_D/W'_D levels converge as the filament size decreases. At the strain rate of 2000 s^{-1}, W_D/W'_D is ~6.5 for the filament size of 1.2 mm and increases slightly by only ~1% as the filament size decreases to 0.8 mm. However, this ratio decreases by 9% as the filament size increases to 1.6 mm. This observation shows that the dissipation tends to plateau as the filament size decreases below 1.2 mm.

4.6 Effect of Microstructure Attributes on Dissipation. Figure 19 compares the ratios of overall plasticity, friction, and damage dissipations in the AM samples with that in the homogenous sample for all simulation sets. The values correspond to a 35% overall compression. The normalization with respect to the homogenous case provides an opportunity for comparing the effects of microstructure attributes. Figure 19(*a*) shows the normalized levels of dissipations for various loading orientations with respect to the filament direction. Except for 0 deg (loading along the filaments), the ratio for plastic dissipation (W_P/W'_P) is lower than unity. The ratios for damage and friction dissipations reach the highest values of 5.49 and 2.79, respectively, when the loading is at 45 deg. Although damage dissipation for 0 deg is significantly higher than that for the homogenous sample ($W_D/W'_D = 4.4$), the corresponding frictional dissipation is lower ($W_F/W'_F = 0.72$).

Figure 19(*b*) compares normalized dissipation levels for porosities in the range of 0–6%. Both W_F/W'_F and W_D/W'_D increase but W_P/W'_P decreases as the porosity increases. This interplay between damage and plasticity results from the fact that higher porosities increase damage and result in lower levels of overall

Table 3 Inter-filament property sets

Property set	ρ (gr/cm^3)	E (GPa)	σ_c (MPa)	ε_c (%)	$\bar{\varepsilon}_D^{pl}$(%)	$\delta_f = L_E \cdot \bar{\varepsilon}_f^{pl}$(mm)	$R = \dfrac{\bar{\varepsilon}_f^{pl}\|_{Interfaces}}{\bar{\varepsilon}_f^{pl}\|_{Filaments}}$
High strength	1.1	2.5	22.5	0.9	12	0.0188	1.00
Intermediate strength (reference sample)	1.1	2.5	22.5	0.9	8	0.0125	0.67
Low strength	1.1	2.5	22.5	0.9	4	0.0063	0.34

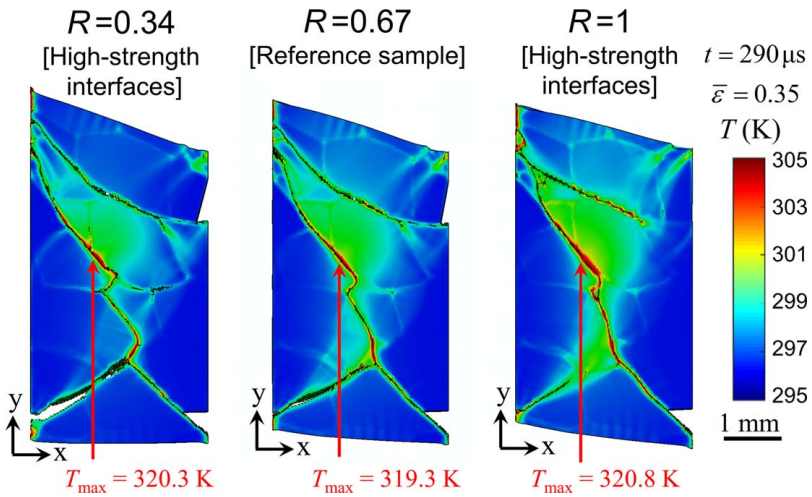

Fig. 14 Temperature fields in the samples with various inter-filament strength levels at $\bar{\varepsilon} = 0.35$ and $t = 290\ \mu s$

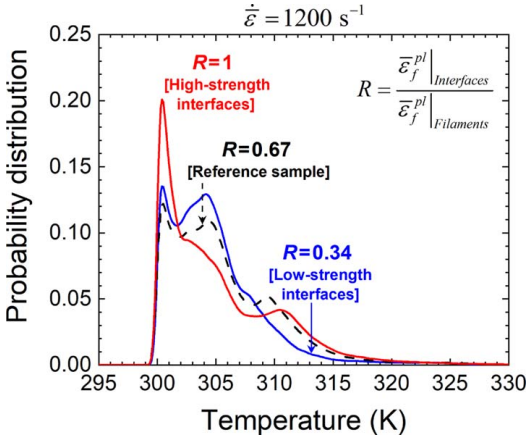

Fig. 15 Comparison of temperature distributions in the samples with various inter-filament strength levels at $\bar{\varepsilon} = 0.35$

stress and plastic dissipation. At 0% porosity, W_F/W'_F and W_D/W'_D are the lowest at 2.01 and 4.54, respectively. At 6% porosity, W_F/W'_F and W_D/W'_D increase to 2.6 and 4.96, respectively. Figure 19(*c*) shows dissipations for the samples with filament sizes of 0.8–1.6 mm. While W_P/W'_P increases, both W_F/W'_F and W_D/W'_D decrease as the filament size increases. The samples with smaller filament sizes have higher densities of inter-filament surfaces and undergo more damage and fracture. The results show that the dissipations plateau as the filament size decreases below ~1 mm. For the filament size of 1.6 mm, W_F/W'_F and W_D/W'_D are the lowest at 2.15 and 4.94, respectively. For the filament size of 0.8 mm, W_F/W'_F and W_D/W'_D are highest at 2.77 and 5.37, respectively.

Finally, Fig. 19(*d*) shows the normalized dissipations as functions of inter-filament strength. Damage and plasticity exhibit opposite trends as the inter-filament strength increases, with W_P/W'_P increases, but W_F/W'_F and W_D/W'_D decrease. When the inter-filament surfaces are as strong as the filaments ($R = 1$), W_F/W'_F and W_D/W'_D are 1.89 and 4.71, respectively. For the low-strength

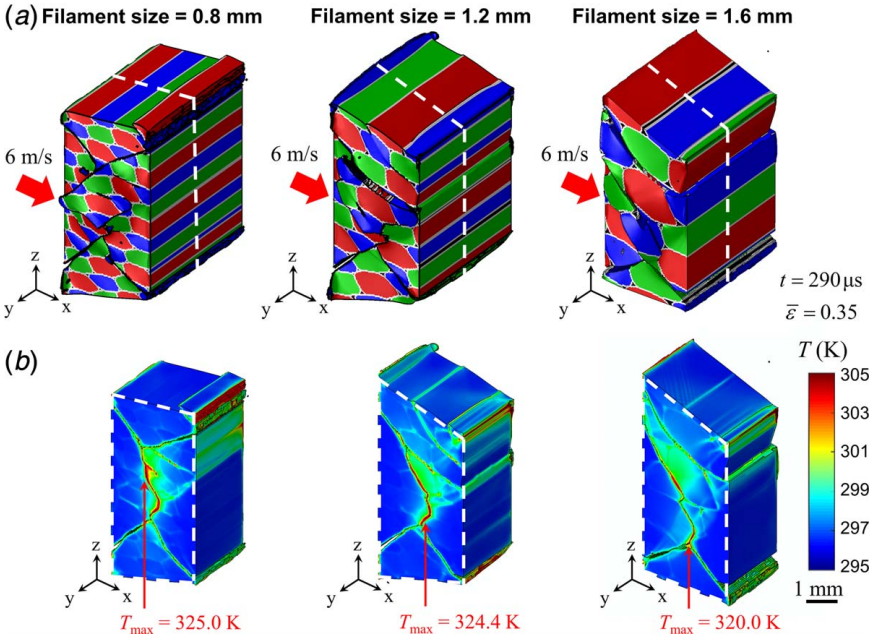

Fig. 16 (*a*) Fracture patterns and (*b*) temperature distributions in the samples with filament sizes of 0.8–1.6 mm at $\bar{\varepsilon} = 0.35$

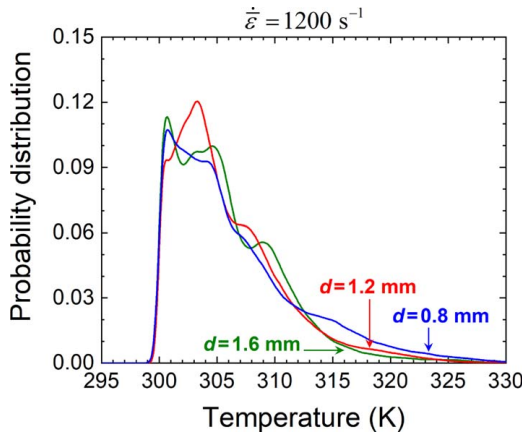

Fig. 17 Temperature distributions in the samples with filament sizes of 0.8–1.6 mm at $\bar{\varepsilon} = 0.35$

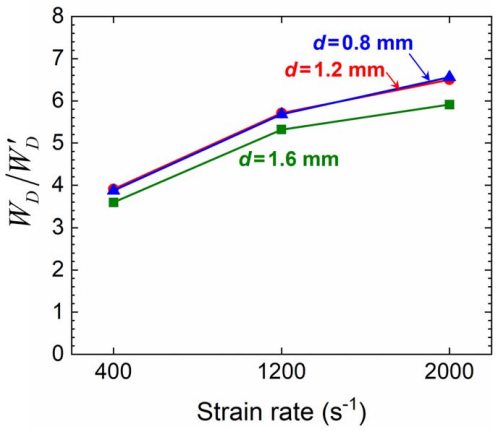

Fig. 18 Ratio of damage dissipation in the AM samples to that in the homogenous sample (W_D/W'_D) as a function of strain rate and filament size at $\bar{\varepsilon} = 0.35$

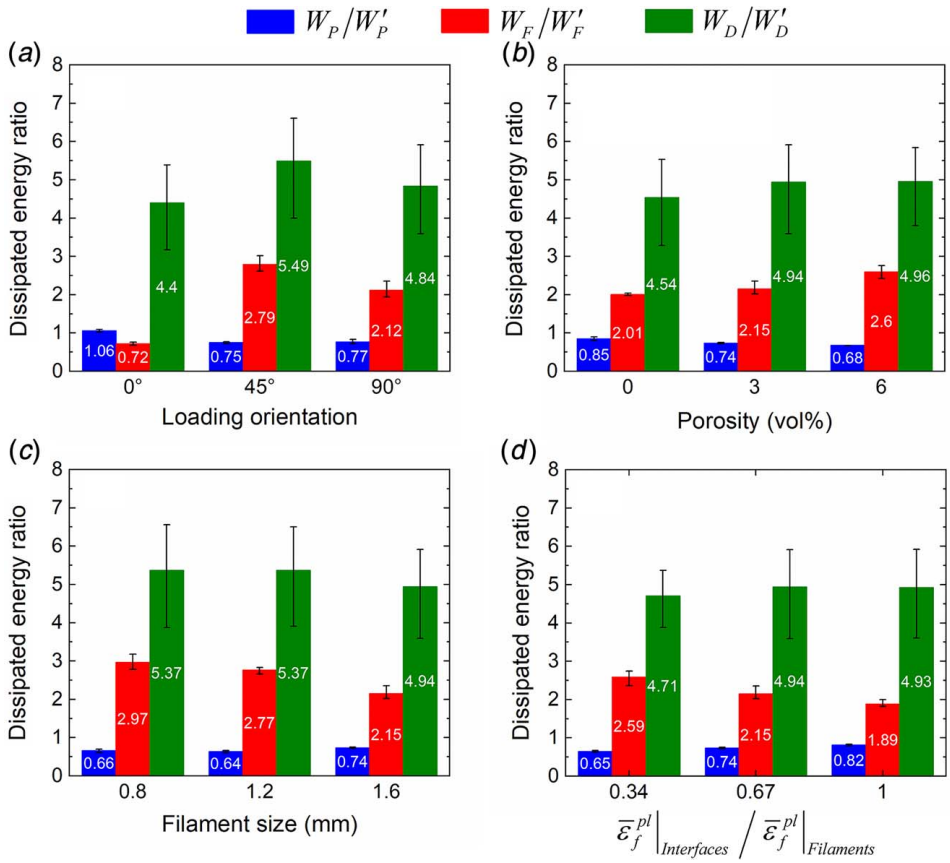

Fig. 19 Ratios of overall dissipated energy in the AM samples to that in the homogenous sample as functions of (*a*) loading orientation, (*b*) porosity, (*c*) filament size, and (*d*) interfacial strength at $\bar{\varepsilon} = 0.35$

inter-filament surfaces ($R = 0.34$), W_F/W'_F and W_D/W'_D are highest at 2.59 and 4.93, respectively.

5 Conclusion

Simulations are performed to analyze the thermo-mechanical response to dynamic loading of a photopolymer-particulate composite which is considered as an AMEM simulant. This material is direct-ink-written in a unidirectional manner. The computations explicitly account for the print structure, with the underlying composite represented with a homogenized constitutive model. Deformation, failure, and heating at the mesoscale are analyzed. To achieve this, an experimentally informed Lagrangian finite element framework is developed, accounting for finite-strain elastic–plastic deformation, strain-rate effect, arbitrary failure initiation and propagation, post-failure contact and friction, heat generation resulting from friction and inelastic bulk deformation, and heat conduction. The samples generated mimic scanned morphologies of the actual materials used in experiments. Three sets of simulations are performed to quantify the effects of print structure, defects (voids and interfaces), and filament size on energy dissipations associated with different mechanisms, hotspot development, and overall stress evolution.

Loading is at strain rates of 400–2000 s^{-1} and emulates the conditions of experiments carried out on a split-Hopkins pressure bar or Kolsky bar. Inelastic and frictional dissipations increase as the loading rate increases. Frictional dissipation is more sensitive to the loading rate than plastic dissipation. Among all orientations, loading in the filament direction results in less damage and higher stresses. In contrast, loading at 45 deg with respect to the filament direction (*xy*-diagonal direction) yields more intense shear bands and the highest temperatures. In comparison with a homogenous sample, the AM samples experience ~3.9 times higher damage dissipation at all loading directions. Frictional dissipation significantly depends on the loading direction and is ~28% lower in the filament direction and ~146% higher in the other directions relative to a homogeneous sample. Although friction contributes only $1-4\%$ of the total heating, frictional heating is localized at fracture sites and plays a vital role in the development of hotspots along shear bands. Voids tend to cause damage initiation at earlier stages of deformation. Higher porosities also result in larger hotspots at higher temperatures. Somewhat counterintuitively, higher inter-filament strength leads to larger hotspots at higher temperatures due to more intense frictional dissipation at higher internal stresses. Finally, smaller filament sizes cause higher levels of damage and higher dissipation due to interfacial friction.

The findings of this study establish trends in and quantification of the relations between structure and response of a class of additively manufactured photopolymer-particulate composites.

Acknowledgment

The authors gratefully acknowledge support from DTRA through Project No. HDTRA1-18-1-0004.

Conflict of Interest

There are no conflicts of interest.

Data Availability Statement

The datasets generated and supporting the findings of this article are obtainable from the corresponding author upon reasonable

request. The authors attest that all data for this study are included in the paper.

Nomenclature

k = thermal conductivity
p = pressure
t = time
L = instantaneous length of sample
E = Young's modulus
c_v = specific heat
v_{rel} = relative sliding velocity
E_m = internal energy per unit mass
L_E = characteristic length of elements
L_0 = initial length of sample
U_s = shock velocity
U_p = particle velocity
W_D = damage dissipation
W_f = frictional dissipation
W_P = plastic dissipation
c_0, s = constants in $U_s - U_p$ linear relationship
β = friction angle of the material in the meridional stress plane
δ_f = equivalent displacement at failure
ΔL = $L - L_0$
$\bar{\varepsilon}$ = overall strain, $\Delta L/L_0$
ε_c = yield strain in compression
$\bar{\varepsilon}_D^{pl}$ = equivalent plastic strain at onset of damage
$\bar{\varepsilon}_f^{pl}$ = equivalent plastic strain at failure
Γ_0 = Grüneisen's gamma at reference state
μ = coefficient of friction
ρ = mass density
ρ_0 = initial mass density
$\boldsymbol{\sigma}$ = Cauchy stress tensor
σ_c = yield stress in compression
σ_e = von Mises equivalent stress
σ_H = hydrostatic stress
σ_n = normal stress
σ_t = yield stress in tension

References

[1] Wong, K. V., and Hernandez, A., 2012, "A Review of Additive Manufacturing," ISRN Mech. Eng., **2012**, pp. 1–10.
[2] Murray, A. K., Isik, T., Ortalan, V., Gunduz, I. E., Son, S. F., Chiu, G. T.-C., and Rhoads, J. F., 2017, "Two-Component Additive Manufacturing of Nanothermite Structures via Reactive Inkjet Printing," J. Appl. Phys., **122**(18), p. 184901.
[3] Muravyev, N. V., Monogarov, K. A., Schaller, U., Fomenkov, I. V., and Pivkina, A. N., 2019, "Progress in Additive Manufacturing of Energetic Materials: Creating the Reactive Microstructures With High Potential of Applications," Propellants, Explos., Pyrotech., **44**(8), pp. 941–969.
[4] Fleck, T. J., Murray, A. K., Gunduz, I. E., Son, S. F., Chiu, G. T. C., and Rhoads, J. F., 2017, "Additive Manufacturing of Multifunctional Reactive Materials," Addit. Manuf., **17**, pp. 176–182.
[5] Ruz-Nuglo, F., Groven, L., and Puszynski, J. A., 2014, "Additive Manufacturing for Energetic Components and Materials," Proceedings of 50th AIAA/ASME/SAE/ASEE Joint Propulsion Conference, Cleveland, OH, July 28–30, p. 3894.
[6] Huang, C., Jian, G., DeLisio, J. B., Wang, H., and Zachariah, M. R., 2015, "Electrospray Deposition of Energetic Polymer Nanocomposites With High Mass Particle Loadings: A Prelude to 3D Printing of Rocket Motors," Adv. Eng. Mater., **17**(1), pp. 95–101.
[7] Clark, B., Zhang, Z., Christopher, G., and Pantoya, M. L., 2017, "3D Processing and Characterization of Acrylonitrile Butadiene Styrene (ABS) Energetic Thin Films," J. Mater. Sci., **52**(2), pp. 993–1004.
[8] Wang, H., DeLisio, J. B., Jian, G., Zhou, W., and Zachariah, M. R., 2015, "Electrospray Formation and Combustion Characteristics of Iodine-Containing Al/CuO Nanothermite Microparticles," Combust. Flame, **162**(7), pp. 2823–2829.
[9] Wang, H., Jian, G., Egan, G. C., and Zachariah, M. R., 2014, "Assembly and Reactive Properties of Al/CuO Based Nanothermite Microparticles," Combust. Flame, **161**(8), pp. 2203–2208.
[10] Ihnen, A. C., Lee, W. Y., Fuchs, B., Petrock, A. M., and Stec, D., III, 2016, "Ink Jet Printing and Patterning of Explosive Materials," Stevens Institute of Technology, US Secretary of Army, U.S. Patent No. 9,296,241 B1.
[11] Tappan, A. S., Ball, J. P., and Colovos, J. W., 2012, "Inkjet Printing of Energetic Materials: Sub-Micron Al/MoO3 and Al/Bi2O3 Thermite," Sandia National Laboratories Presentation SAND2011-8957C, Albuquerque, NM.
[12] McClain, M., Gunduz, I., and Son, S., 2019, "Additive Manufacturing of Ammonium Perchlorate Composite Propellant With High Solids Loadings," Proc. Combust. Inst., **37**(3), pp. 3135–3142.
[13] Lewis, J. A., 2006, "Direct Ink Writing of 3D Functional Materials," Adv. Funct. Mater., **16**(17), pp. 2193–2204.
[14] Stansbury, J. W., and Idacavage, M. J., 2016, "3D Printing With Polymers: Challenges Among Expanding Options and Opportunities," Dent. Mater., **32**(1), pp. 54–64.
[15] Oropallo, W., and Piegl, L. A., 2016, "Ten Challenges in 3D Printing," Eng. Comput., **32**(1), pp. 135–148.
[16] Lee, C., Kim, S., Kim, H., and Ahn, S., 2007, "Measurement of Anisotropic Compressive Strength of Rapid Prototyping Parts," J. Mater. Process. Technol., **187**, pp. 627–630.
[17] Ahn, S.-H., Montero, M., Odell, D., Roundy, S., and Wright, P. K., 2002, "Anisotropic Material Properties of Fused Deposition Modeling ABS," Rapid Prototyp. J., **8**(4), pp. 248–257.
[18] Mueller, A., Schmalzer, A., Bowden, P., Tappan, B., White, A., and Menikoff, R., 2019, "Diameter Effects on the Directional Anisotropic Detonation Behavior of Strand Structured Additively Manufactured Explosives," 21st Biennial Conference of the APS Topical Group on Shock Compression of Condensed Matter, Portland, OR, June 16–21, Vol. 64.
[19] O'Grady, C., Tappan, A., Knepper, R., Rupper, S., Vasiliauskas, J., and Marquez, M., 2019, "Investigating Typical Additive Manufacturing Defect Geometries Using Physical Vapor Deposition Explosives as a Model System," 21st Biennial Conference of the APS Topical Group on Shock Compression of Condensed Matter, Portland, OR, June 16–21, Vol. 64.
[20] Keyhani, A., Kim, S., Horie, Y., and Zhou, M., 2019, "Energy Dissipation in Polymer-Bonded Explosives With Various Levels of Constituent Plasticity and Internal Friction," Comput. Mater. Sci., **159**, pp. 136–149.
[21] Field, J., Bourne, N., Palmer, S., Walley, S., Sharma, J., and Beard, B., 1992, "Hot-Spot Ignition Mechanisms for Explosives and Propellants [and Discussion]," Philos. Trans. R. Soc., A, **339**(1654), pp. 269–283.
[22] Hong, S. Y., Kim, Y. C., Wang, M., Kim, H.-I., Byun, D.-Y., Nam, J.-D., Chou, T.-W., Ajayan, P. M., Ci, L., and Suhr, J., 2018, "Experimental Investigation of Mechanical Properties of UV-Curable 3D Printing Materials," Polymer, **145**, pp. 88–94.
[23] Zhang, P., and To, A. C., 2016, "Transversely Isotropic Hyperelastic-Viscoplastic Model for Glassy Polymers With Application to Additive Manufactured Photopolymers," Int. J. Plast., **80**, pp. 56–74.
[24] Arruda, E. M., and Boyce, M. C., 1993, "Evolution of Plastic Anisotropy in Amorphous Polymers During Finite Straining," Int. J. Plast., **9**(6), pp. 697–720.
[25] Arruda, E. M., and Boyce, M. C., 1993, "A Three-Dimensional Constitutive Model for the Large Stretch Behavior of Rubber Elastic Materials," J. Mech. Phys. Solids, **41**(2), pp. 389–412.
[26] Wagner, K. B., Keyhani, A., Boddorff, A. K., Kennedy, G., Montaigne, D., Jensen, B. J., Beason, M., Zhou, M., and Thadhani, N. N., 2020, "High-Speed X-ray Phase Contrast Imaging and Digital Image Correlation Analysis of Microscale Shock Response of an Additively Manufactured Energetic Material Simulant," J. Appl. Phys., **127**(23), p. 23.
[27] Keyhani, A., and Zhou, M., 2020, "Thermo-Mechanical Response of an Additively Manufactured Energetic Material Simulant to Dynamic Loading," Submitted for publication.
[28] Keyhani, A., Yang, R., and Zhou, M., 2019, "Novel Capability for Microscale In-Situ Imaging of Temperature and Deformation Fields Under Dynamic Loading," Exp. Mech., **59**(5), pp. 1–16.
[29] Qu, J., and Cherkaoui, M., 2006, *Fundamentals of Micromechanics of Solids*, Wiley, Hoboken, NJ, pp. 120–153.
[30] Zhou, M., Ravichandran, G., and Rosakis, A. J., 1996, "Dynamically Propagating Shear Bands in Impact-Loaded Prenotched Plates—II. Numerical Simulations," J. Mech. Phys. Solids, **44**(6), pp. 1007–1032.
[31] Drucker, D., 1973, "Plasticity Theory Strength-Differential (SD) Phenomenon, and Volume Expansion in Metals and Plastics," Metall. Trans., **4**(3), p. 667.
[32] Seltzer, R., Cisilino, A. P., Frontini, P. M., and Mai, Y.-W., 2011, "Determination of the Drucker–Prager Parameters of Polymers Exhibiting Pressure-Sensitive Plastic Behaviour by Depth-Sensing Indentation," Int. J. Mech. Sci., **53**(6), pp. 471–478.
[33] Hooputra, H., Gese, H., Dell, H., and Werner, H., 2004, "A Comprehensive Failure Model for Crashworthiness Simulation of Aluminium Extrusions," Int. J. Crashworthiness, **9**(5), pp. 449–463.
[34] Pijaudier-Cabot, G., and Bazant, Z. P., 1987, "Nonlocal Damage Theory," J. Eng. Mech., **113**(10), pp. 1512–1533.
[35] Comi, C., 2001, "A Non-Local Model With Tension and Compression Damage Mechanisms," Eur. J. Mech. A Solids, **20**(1), pp. 1–22.
[36] Prakash, C., Gunduz, I. E., Oskay, C., and Tomar, V., 2018, "Effect of Interface Chemistry and Strain Rate on Particle-Matrix Delamination in an Energetic Material," Eng. Fract. Mech., **191**, pp. 46–64.
[37] Olokun, A., Li, B., Prakash, C., Men, Z., Dlott, D. D., and Tomar, V., 2019, "Examination of Local Microscale-Microsecond Temperature Rise in HMX-HTPB Energetic Material Under Impact Loading," JOM, **71**(10), pp. 3531–3535.